Temporal GPR imaging of an ethanol release within a laboratory-scaled sand tank

D. R. Glaser[1], D. D. Werkema[2], R. J. Versteeg[3], R.D. Henderson[4,5], and D.F. Rucker[6]

[1]*Washington River Protection Solutions, LLC., Contractor to the Department of Energy, Richland, WA., 99352*

[2]*U.S. EPA, Office of Research & Development, National Exposure Research Laboratory, Las Vegas, NV 89119*

[3] *Subsurface Insights, LLC., Hanover, NH,03755*

[4]*University of Connecticut, Center for Integrative Geosciences, Storrs, CT, 06269*

[5]*U.S. Geological Survey, Office of Groundwater, Branch of Geophysics, Storrs, CT, 06269*

[6]*hydroGEOPHYSICS, Inc., Tucson, AZ, 85745*

Abstract

Within the last decade efforts in geophysical detection and monitoring of fossil fuel releases into the subsurface have shown increasing success, including the ability to geophysically detect and delineate enhanced and natural biodegradation and remediation activities. The substitution of biofuels, such as ethanol, for fossil fuels is becoming persistent in the national and international marketplace making it subject to the same types of accidental releases and exposure scenarios currently associated with the transport and storage of fossil fuels. Thus, there is interest from both academics and regulators to investigate the feasibility of applying geophysical methodologies to biofuel releases. In this study, we performed an experimental and numerical

investigation of the feasibility of using ground penetrating radar (GPR) to monitor the migration of an ethanol release. A tank scale model of a closed hydrologic system was prepared with Ottawa sand and instrumented with an automated gantry measurement apparatus for time-lapse measurement of zero offset and coincident GPR reflections on multiple horizontal planes. Measurements were acquired in the unsaturated and saturated zones throughout the injection and transport of the ethanol release. The results of the monitoring suggest a measureable contrast within both time and frequency domains of the GPR data coincident with the ethanol release and subsequent migration. We conclude that the monitoring of ethanol in a sand matrix at various levels of saturation is possible with GPR.

Keywords: GPR, ethanol, biofuels

1.0 Introduction

Ethanol use has grown in recent years due in large part to its inclusion in fuels as an emissions reducing fuel oxygenate. The additional draw to ethanol has been to replace methyl tertiary-butyl ether (MTBE) as a fuel oxygenate in reformulated gasoline (up to 10 percent by volume in gasoline) due to the solubility of MTBE in groundwater and its carcinogenic effects (Wheals et al., 1999). "Flex Fuel" vehicles utilizing E85 (85 percent ethanol, 15 percent gasoline) have also contributed to the use and distribution of ethanol. While ethanol is not considered to be directly harmful to human health, its use has indirect consequences through secondary environmental effects.

The potential for ethanol to also impact groundwater has been the focus of many studies in recent years. Researchers have found the addition of ethanol to the subsurface in the presence of

benzene, toluene, ethylbenzene, and xylenes (BTEX) reduces natural attenuation of the harmful BTEX compounds because ethanol is preferentially biodegraded (Corseuil et al., 1998; Ruiz-Aguilar et al., 2003; Powers et al., 2001; MacKay et al., 2006). Additionally, ethanol has cosolvency effects on existing non-aqueous phase liquids (NAPL) allowing transport and partitioning of harmful and otherwise immobile chemicals in the subsurface (Da Silva et al., 2002; McDowell et al., 2003; Gomez & Alvarez, 2009; Frietas, 2009). Gasoline mixed with ethanol has also been shown to penetrate clay layers that would otherwise be impenetrable to gasoline alone (Stallard et al., 1997). Multiple studies have shown the degradation of ethanol to result in methane production at potentially hazardous levels (MacKay et al. 2006; Frietas et al., 2010a; Frietas et al., 2010b).

Physical property differences between ethanol and water suggest geophysical imaging methods such as resistivity, induced polarization, and high frequency electromagnetic methods can provide a means of differentiating between water-saturated pore spaces and ethanol-saturated pore spaces in the subsurface (McNaughton et al., 2009; Henderson et al., 2010; Glaser et al., 2010; Personna et al., 2011a; Personna et al., 2011b ; Glaser et al., 2011). Lucius et al. (1992) showed ethanol to be miscible in water, with a density of 0.79, a relative dielectric permittivity (dielectric) of 25 (at 20 deg C), and a frequency dependent response. When compared with the dielectric of water (80), there should be sufficient contrast to detect the presence of ethanol (Glaser et al., 2010; Henderson et al., 2010; Glaser et al., 2011). Additionally, even though ethanol is known to be miscible in water, laboratory experiments have shown that the ethanol can be retained within the capillary fringe rather than infiltrating to the saturated zone (Frietas and Barker, 2009; Glaser et al., 2010; Henderson et al., 2010; Glaser et al., 2011). A reduced dielectric permittivity should be observed in areas where ethanol and water readily mix, while

areas previously occupied by air (dielectric of 1) in the pore-space should also demonstrate an increase in the dielectric due to the wetting of pore space by the ethanol (Hagrey and Müller, 2000; Farmani et al., 2008).

In this work we investigated an ethanol release with ground penetrating radar (GPR), with the main objective to demonstrate that the method is capable of discerning the movement of ethanol within a sandy host environment. GPR is a high resolution electromagnetic geophysical method capable of discerning contrasts in bulk dielectric based on varying volumetric mixtures of soil, air, water, and ethanol. The release was conducted in a highly controlled setting, i.e., a sand tank with known geometrical, hydrological, and electrical parameters (Birken and Versteeg, 2000; Versteeg and Birken, 2001; Versteeg, 2004; Loeffler and Bano, 2004: Bano, 2006; Mazella and Majer, 2006; Benedetto, 2010). Mixing models and FDTD modeling were also completed in an effort to understand the individual contributions to the resulting GPR profiles from ethanol mixing and tank geometry (Bano et al., 2009). The GPR models were run with different dielectric values to span the range of expected laboratory conditions. For the laboratory experiment, we used variations in reflected electromagnetic wave amplitude, two-way travel time of the wave, and power spectra to make assessments of ethanol in the saturated zone, unsaturated zone, and within the capillary fringe. With this laboratory study, the GPR method will be shown to have sufficient sensitivity to warrant additional investigations at the field scale.

2.0 Ground Penetrating Radar Wave Propagation and Analysis

GPR utilizes electromagnetic radio waves in a frequency range of 50 Mhz - 2 Ghz, which are emitted by a transmitting antenna. The resulting reflected and refracted waves are recorded by a receiving antenna that measures the voltage amplitude over time, called a trace. GPR is used

extensively to investigate both near surface soils as well as a range of engineered structures such as roads and bridges. Propagation and reflection of the radio wave through any medium depends on the dielectric and other electromagnetic properties of the medium.

GPR measurements can be made in a transmission configuration or a reflection configuration. The transmission configuration generally measures the volume of the earth (or sample) located between the two antennas, usually borehole to borehole. The reflection configuration relies on reflections resulting from contrasts in the dielectric properties of the soil for antennas on the same soil plane, for example on the ground surface or within a single borehole.

2.1 Wave Propagation Theory

The propagation of GPR energy into the subsurface can be described using Maxwell's equations (Carcione, 1996; and Greaves et al., 1996). The factors which control the arrival time and shape of the waveform are the velocity and attenuation of the wave in the medium (Davis and Annan, 1989). The velocity (V_m) of radio waves is dependent upon the relative dielectric permittivity (ε_r) and the relative magnetic permeability (μ_r) in proportion to the speed of light in free space (c = 299.8 mm/ns):

$$V_m = \frac{c}{\sqrt{\left[\left(\frac{\varepsilon_r \mu_r}{2}\right) \times \left[\left(+P^2\right) + 1\right]\right]}} \qquad (1)$$

where the loss factor is represented by P, generally expressed as:

$$P = \frac{\sigma}{\left(2\pi f\right) \times \left(\varepsilon_r \varepsilon_0\right)} \qquad (2)$$

Frequency is denoted as *f*, σ is the electrical conductivity, and ε_0 is the dielectric permittivity of free space (8.854 x 10^{-12} F/m). In non-magnetic materials, μ_r is approximately 1 (Reynolds, 1997). Equations 1 and 2 are valid only for real values of permittivity and conductivity. Furthermore, Davis and Annan (1989) show that in low-loss geologic materials, P is approximately zero, reducing Equation 1 to:

$$V_m = \frac{c}{\sqrt{\varepsilon_r}} \tag{3}$$

For heterogeneous materials of contrasting dielectric values, a reflection coefficient (R) at a given interface with no signal loss, and for the case of normally incident signal only, is quantified by (Conyers and Goodman, 1997):

$$R = \frac{\sqrt{\varepsilon_a} - \sqrt{\varepsilon_b}}{\sqrt{\varepsilon_a} + \sqrt{\varepsilon_b}} \tag{4}$$

where the relative dielectric constants of the layer on either side of the interface are represented by ε_a and ε_b, respectively. The transmission coefficient, T, is simply:

$$T = 1 - R \tag{5}$$

It is important to note the transmission coefficient calculation as presented is also only valid for vertically incident waves. GPR signals are attenuated through multiple mechanisms. Every reflection at a dielectric interface results in some loss of energy available for the deeper reflections, thus attenuating the signal (Reynolds, 1997). Signal loss due to refraction along a high velocity interface, such as that of air and the ground surface, can also occur (Rucker and Ferré, 2003). Additional modes of signal loss include: signal scattering due to inhomogeneities

within the medium (Doolittle and Collins, 1995; Benedetto, 2010); scattering from thin layers or point sources like cobbles (Davis and Annan, 1989); objects that have dimensions comparable to the signal wavelength, i.e., Mie scattering (Reynolds, 1997; Bano, 2006), or the many facets of pore specific conditions, including but not limited to, pore structure, pore shape, pore fluid distribution, and pore fluid chemistry (Sen et al., 1981; Sen et al., 1984; Kenyon, 1984; Shen et al., 1985; Tyc et al., 1988; Friedman, 1998; Jones and Friedman, 2000; Cosenza et al., 2003; Chen and Or, 2006; and Endres and Bertrand, 2006).

The frequency-dependent attenuation factor (α) provides the attenuation for a specific frequency for a given medium with known conductivity, magnetic permeability , and dielectric properties is represented by:

$$\alpha = 2\pi f \left\{ \left(\frac{\varepsilon_r \mu_r}{2} \right) \left[\left(1 + \frac{\sigma^2}{(2\pi f)^2 \times \varepsilon_r^2} \right)^{1/2} - 1 \right] \right\}^{1/2} \tag{6}$$

Again, assuming a low loss medium, Davis and Annan (1989) show that equation (6) can be simplified as:

$$\alpha = \frac{(1.69 \times 10^3) \cdot \sigma}{\sqrt{\varepsilon_r}} \tag{7}$$

The attenuation factor is given in dB/m, and gives the rate at which electromagnetic energy is dissipated into the ground. Additionally, the wave amplitude will decrease inversely with distance from the source due to geometric spreading (Annan, 2001). Since the presence of pore water will affect both the dielectric and the conductivity of the medium, the attenuation factor of a soil has been used to estimate soil water content (Olver and Cuthbert, 1988). Within the

context of this study, the relative attenuation factor differences and reflection amplitude values are likely to be the most descriptive variables for detecting the presence (or absence) of ethanol throughout the soil column.

2.2 Sensitivity of GPR to the Detection of Ethanol within the Vadose and Saturated Zones

To demonstrate the sensitivity of the GPR method, synthetic models were generated for a series of binary layered systems. The models were conducted to understand expected response from both the relative attenuation factor and reflection amplitude and whether GPR could be used to discern an ethanol release. Table 1 displays the geoelectrical variables (dielectric and electrical conductivity) taken from Wightman et al. (2003) and Werkema et al. (2010), as well as the wave propagation variables (velocity and calculated attenuation factor) associated with the individual constituents of the synthetic model demonstration. Air, water, and ethanol values are presented independent of a sand matrix in an attempt to understand the contributions of each component prior to the effects of their interactions. The dielectric of dry, moist, and wet sand mixtures were calculated from a modified Topp's equation (Rucker and Ferré, 2004), assuming a 3%, 20%, and 40% moisture content by volume, respectively. Porosity was also assumed to be 40%.

Table 2 lists the various interface models and values from which the reflection coefficients were calculated. Conditions A through F examine simple comparisons between a soil and a pure fluid, including a dry and wet sand with water, air, or ethanol. Conditions G through J focuses on two different soils for which the pore space is occupied by air, air and ethanol, air and water, or air, water, and ethanol. Additionally, for these last set of conditions, three mixing models are used to estimate the dielectric, namely the parallel, cubic, and Complex Refractive Index Model (CRIM) mixing models. The mixing models represent varying levels of complexity, accounting for

additional geometric and geologic parameters as we increase from parallel to CRIM. The parallel mixing model is based on Maxwell's equations (Borrow et al., 1997; Yoon et al., 2003):

$$\varepsilon_r = V_a \varepsilon_a + V_b \varepsilon_b \tag{8}$$

where ε_r is the estimated relative dielectric, V_a and V_b are the volume fractions of material a and b respectively, while ε_a and ε_b are the dielectric of the two materials. The cubic mixing model is used in an attempt to better compensate for fluid mixtures dispersed into the soil grains, accounting for both parallel and series mixing geometries (Borrow et al., 1997; Orbey and Sandler, 1998; Yoon et al., 2003):

$$\varepsilon_c = \frac{\varepsilon_a \varepsilon_b}{(\varepsilon_b - \varepsilon_a) V_a^{-1/3} + \varepsilon_a V_a^{-2/3}} + \varepsilon_b (1 - V_a^{2/3}) \tag{9}$$

Both the parallel and cubic mixing models allow for only two phases. To model greater than two phases the models were nested within the models, i.e., the relative dielectric permittivity was calculated for the mixing of water and ethanol, and the resulting value was then used in the mixing of water /ethanol with the silica matrix. This approach produced reasonable values; however, the CRIM is widely held as an industry standard for 1D GPR modeling, and specifically differentiates between pore space and matrix, allowing for multiphase mixing (Roth et al., 1990; Endres and Knight, 1992):

$$\varepsilon_r = \left[\sum_{i=1}^{N} f_i \sqrt{\varepsilon_i} \right]^2 \tag{10}$$

For the case of a three phase mineral/water/NAPL mixture, Ajo-Franklin et al. (2004) describe CRIM as:

$$\varepsilon_r = \left[\phi\left(S_w\sqrt{\varepsilon_w} + S_e\sqrt{\varepsilon_e}\right) + (1-\phi)\sqrt{\varepsilon_m}\right]^2 \qquad (11)$$

In this study the NAPL component is replaced by ethanol. As we were working in both saturated and unsaturated conditions our modeling attempts to use a four phase system additionally accounting for the presence of air in the pore space:

$$\varepsilon_r = \left[\phi\left(S_w\sqrt{\varepsilon_w} + S_e\sqrt{\varepsilon_e} + S_a\sqrt{\varepsilon_a}\right) + (1-\phi)\sqrt{\varepsilon_m}\right]^2 \qquad (12)$$

where the total effective dielectric constant (ε_r) is estimated from the relative proportion of variables within the pore space (ϕ) to that of the matrix (1-ϕ). Within the first term we account for the individual constituents of the pore space, namely: water (*w*), ethanol (*e*), and air (*a*). The second term of Equation 12 accounts for the contribution from the soil matrix (*m*). The three mixing models will provide similar relative dielectric values for conditions where the dielectric of each individual material is also similar. For greater differences in dielectric, the cubic mixing model produces a lower value.

Table 2 displays the dielectric and wave velocity values for each medium. From these, reflection and transmission coefficients are calculated. We chose to present the absolute value of the reflection coefficient to highlight the general strength of received wave. Wherever ethanol is indicated in the table, values are based on a combination of ethanol with a common tracer dye known as Brillant Blue FCF (BB). BB was added to the ethanol in the sand tank experiment in an effort to visualize its movement through the subsurface. Confirmation of the GPR interpretations was conducted through time-lapse photography, which captured conditions at a rate of 1 image per 1 minute interval. Adding the dye enhanced the visualization, but changed the electrical conductivity of the mixture from 2.5 x 10^{-8} S/m to 1.5 x 10^{-7} S/m. While this

represents a change in electrical conductivity of more than an order of magnitude, the change in dielectric constant is negligible compared to the range of the other model components.

Conditions A through C of Table 2 represent the basic components in the unsaturated zone. In each of these combinations a high reflection coefficient is shown, which suggests an interface composed of a dry sand and a pure fluid would provide a strong reflection. To help compare the reflection coefficient among the different conditions, a fuzzy rating system was developed based on each reflection coefficient as to whether the target interface is of a good quality, i.e. is the reflected amplitude of sufficient intensity to likely be observed in a GPR trace. The ratings for the various conditions, shown visually in Figure 1, consist of Poor (≤0.10), Good (0.10-0.30), Very Good (0.30-0.50), and Excellent (0.50-1.00), and based on the authors' prior experience with GPR. Conditions A through C demonstrate qualities of good, very good, and excellent, respectively.

The saturated zone is represented by wet sand in conditions D through F. The results indicate that the interface between wet sand and air should be an excellent target while the wet sand and pure ethanol interface is a poor reflector and not likely to be detected given the similar dielectric values.

Estimates of more realistic interface properties are shown in conditions G through J representing a sand matrix with variable volume fractions of air, water, and ethanol. The dielectric constants are calculated based on the parallel, cubic , and CRIM models. For instance, conditions G_p ,$G_{c,}$, and G_{crim} examines a target interface between a dry sand and a dry sand with 20% ethanol. Regardless of the mixing model, the estimated quality of this reflected target is good. Condition $H_{(p,c,crim)}$ represents the introduction of ethanol above the capillary fringe, where moist sand and

sand with approximately half the pore space occupied by ethanol is tested. Depending on the mixing model, the quality of the target is either poor or good. The latter is due to the cubic mixing model having a slightly lowered dielectric for the ethanol mix. Given the greater complexity of the cubic model, we assume accounting for the additional geometry within the mixing model should result in a more accurate prediction of target quality. Lastly, conditions $I_{(p,c,crim)}$ and $J_{(p,c,crim)}$ are most similar to the introduction of ethanol into the saturated zone. If the ethanol displaces water and occupies a large portion of the pore space (condition I), then the reflection amplitudes are higher and target qualities are good. However, if the ethanol is diffuse with a lower volume fraction, the target quality is quite poor. In summary, conditions $G_{p,c,crim}$ through $J_{p,c,crim}$ suggest that ethanol should be easily detected in the unsaturated soil, less so in a soil with a capillary fringe, and the saturated soil has a low likelihood of detection unless the volume fraction of ethanol is high. With the very basic components modeled here, all three mixing models, from simple to geologically accurate, performed similarly.

3.0 Experimental Methods

3.1 Description of Laboratory Tank Model and Measurement System

A 124 cm x 48 cm x 78 cm glass tank was filled with F-45 Ottawa sand from U.S. Silica (Ottawa, IL), ranging in grain size from 0.1 mm to 0.85 mm. The tank was located within a temperature-controlled laboratory, which remained 21°C +/- 2° C throughout the duration of the experiment. Within the tank, the location for the ethanol release was chosen at an offset location, along the length of the tank, to limit false positives due to GPR reflections received as a result of the tank boundaries. A line-source release point was designed to simulate a pipeline leak, and Figure 2A through 2C show the layout of the tank, release point, and other hydrological

boundaries. The release point consisted of a half-inch diameter PVC pipe centered and leveled within a 10 cm x 48 cm x 10 cm pea gravel trench. The pipe was screened only on the top side with 0.3 cm openings every 1.3 cm along the length of the pipe. This ethanol release design allowed for an even flow of ethanol across the length of the pipe.

For visual observation of the ethanol release and infiltration into the tank, the ethanol was dyed with BB. Koestel et al. (2008) showed that BB can be used as a visual and electrical tracer in electrical resistivity tomography (ERT) experiments. Brilliant Blue is not a perfectly conservative tracer as it has been shown to exhibit retardation in unsaturated flow due to nonlinear absorption to the soil matrices (Flury and Flühler, 1995; Kasteel et al., 2002). However, it is ideal for illustrating water flow pathways in soils (Haarder et al., 2011).

Water was pumped into the tank at an access point screened only within the intended saturated area (approximately 55 liters at a rate of 22 L/h). This resulted in the top of the capillary fringe at 45 cm below the tank's surface (bts), the top of the saturated zone at 55 cm bts, and the bottom of the tank was located at 78 cm bts. It is assumed that the glass tank represents a closed hydrologic system with no influx or outflux of fluid, excepting the ethanol release. The ethanol release point was located at 25 cm bts, and denatured ethanol dyed with Brilliant Blue was pumped via a peristaltic pump into the system at a rate of approximately 1L/hr over 7 hours, resulting in a total of 7 L released into the tank. The injection of ethanol should result in a mounded water table.

A gantry system (Figure 2D) was used to automate the acquisition of GPR data over the injection and recovery period (Versteeg and Birken, 2001; Birken and Versteeg, 2000; Versteeg, 2004). We used two 800 Mhz antennas (combined transmitter and receiver) operated by a Mala CUII

four channel control unit and Mala Groundvision acquisition system. The system is externally controlled by a PC to allow for continuous data acquisition. The multichannel antenna configuration allows the acquisition of four different GPR data sets in a single acquisition run: two reflection datasets, and two transillumination datasets. For the purpose of this discussion, we are limiting the analysis to a fixed-offset reflection dataset. The Mala system also has the capability of geo-referencing the antenna position through serial input from a standard GPS. The antennae position data were sent to the Mala system via the gantry Java control software, which creates a GPS formatted string of the gantry system position data. In this manner the actual position of the antennas during acquisition is integrated with the Mala GPR data acquisition. As currently configured, our system moves in an XZ plane along the tank, as the Y position stays constant.

At the beginning and end of the experiment, a full characterization data set was acquired obtaining twelve profiles where the depth position incrementally increased in steps of 7.5 cm. The characterization dataset took approximately 15 minutes to acquire. For the monitoring data sets during the ethanol release, six equally spaced profiles were acquired in increments of 15 cm. Each monitoring data set required 6 minutes to complete. A total of 154 fixed-offset reflection data files were acquired over the investigation period, which spanned approximately 16.5 hours. For the purpose of visual correlation of results, photographs of the tank side view were acquired at 1 minute interval during the investigation. Finally, it is important to note that the configuration of the antennas in this study most closely represent a borehole field survey rather than a surface field survey, since the measurements are made on the side of the soil column rather than from above. That is the two-way travel time along the y-axis of the GPR data profiles represent GPR travel time propagating horizontally through the side of the tank.

3.2 FDTD Modeling of Laboratory Tank Model

A two-dimensional FDTD ground penetrating radar model was used to track the arrival of reflected and refracted waves at the receiver antenna for the simulated tank environment. The numerical model, developed by Irving and Knight (2006), was chosen for the task based on its ease of use and implementation. The modeling exercise was conducted to demonstrate the potential for refracted and reflected waves along adjacent and far side walls to interfere with direct interpretation of reflections from an ethanol release. Rucker (2011) also found the numerical model useful when evaluating first arrival travel time data from refracted waves in the transmission configuration. Figure 4A shows the dimensions of the simulated tank, which for simplicity, contained a single material of constant dielectric. An 800 MHz pulse was simulated at the transmitter (TX) and the receiver (RX) was stationed nearby to record the incoming waves. To mimic the gantry system, the TX/RX antennas were moved from left to right across the tank. The adjacent and far walls are labeled to help in the discussion for boundary reflection and refraction events. The tank was surrounded by air with a dielectric of one.

Figure 4B through 4D show the results of the received wave for three dielectric values representing dry sand, dry sand with 20% ethanol, and wet sand with 5% ethanol. The results are presented as amplitude of voltage for the electric field. In each example the first wave to arrive is the direct wave through air from TX to RX. In Figure 4B, the next set of arrivals and locations from which the arrivals came are labeled to the left. Based on the two-way travel time, a material of dielectric 3.3 will have a reflection event arrive at 6.05 ns from wall B. At the far left side of the tank, the reflection from wall B and critical refraction along wall A nearly arrive at the same time. As the antennas move closer to the center of the tank, the reflection from wall B is constant while the arrival of the refraction takes longer due to the longer distance traveled.

The strong, high amplitude event at later times represent a refraction from the far wall C. The arrival time from wall C decreases as the antennas move closer to that wall. Multiples are also observed, for example multiple reflections from wall B will occur in integer harmonics of 6.05 ns, but get weaker over time. Lastly, a few side wall reflections are also observed, as their arrivals are hyperbolic in nature. The most notable is the side wall reflection that occurs from wall A immediately after the refraction from wall A. As the antennas move closer to the center, the refraction and reflection arrivals diverge.

As the dielectric increases in value, the intensity of the refracted events decrease. The highest dielectric material in Figure 4D shows only a slight contribution from refraction in early time. In late time, the arrivals appear reflective in nature, albeit weak.

4.0 Results & Discussion

Our discussion focuses on the results from a select data set, which consists of three horizontal profiles at eight times throughout the 17 hour duration of the experiment. Presentation times were selected closer together nearer the injection time and then further apart as time progressed. For reference, Figure 3 shows the locations of the profiles (profiles 9, 21, and 33) overlain on the time-lapse photograph for each selected time, which are labeled A through H. Profile 9 is located within the unsaturated zone, above the capillary fringe and below the injection point. Profile 21 is located within the capillary fringe, and profile 33 is located just below the water table.

Figures 5 through 7 show the results for each of the selected profiles as a series of contoured amplitude plots, and a single trace within the immediate vicinity of the injection point plotted adjacent to each profile. The time axes for each subplot in the figures were corrected to

accommodate a direct arrival from TX to RX with a separation of 0.14 m. The Time A trace, representing the baseline condition prior to the ethanol release, is then compared to traces from each subsequent data acquisition time (B-H), resulting in a direct visual comparison of changes in reflection amplitude and velocity as time progressed.

The data within profile 9 (Figure 5) show several reflections in the first 10 ns from adjacent tank walls, the far tank wall, the top air boundary, and the lower water table boundary. Although the sand in the tank is fairly dry with a low dielectric, there are no obvious refractions from the adjacent walls as seen in the FDTD modeling examples. Understanding the exact boundary for each reflection event is tenuous; however, we estimate the reflection due to effects from the ethanol release start around 7 ns. Before this time, the arrivals remain relatively uniform across the tank and across time, as seen in the marker at 4 ns. The most obvious effects of the release occur immediately after cessation of ethanol release (Figure 5G), where the first half of the tank sees signal dampening between 5 and 10 ns, due to the ethanol loading the water table and subsequent vertical displacement of the groundwater towards the opposite side of the tank. Bano (2006) explains a reduced or nonexistent reflection in transition zones above a water table due to the ratio of transition layer thickness to the wavelength of the signal. Although our data is not acquired with vertical incidence, this can be applied to our results, which indicate a clear target seen from the loading effect within the closed system. Based on hydrological grounds it is reasonable to assume that the mounding will have an increasing moisture content moving from the outside in. This suggests that our transition zone thickness (i.e. the boundary from the saturated portion of the mounding to the unsaturated portion) is less than half that of our dominant wavelength (800 MHz). Signal dampening is also observed along the second half of the time G profile at 14 to 17 ns. The release is at 1.82 m, and traces extracted from this location

show a significant signal dampening and delay relative to background. The dampening at this location seems to begin around time C and then starts to return to background around time H. The greatest change in target strength is observed after the end of the injection. Since this profile is located very near to the injection point, it is reasonable to assume that the response in this region is due to the residual liquid, but is mostly a function of volatilized gas phase ethanol in the pore-space. Variations in pore-space gas content have been shown to affect GPR imaging results.

Figure 6 shows the same series of amplitude contours for profile 21, located just above the water table along the capillary fringe. Again, the first 5 ns of reflection arrivals remain constant throughout the experiment. In fact, no real change in amplitudes occur until about two hours into the release (Figure 6E). Here, we see amplitude dampening along the marker arrivals at around 15 ns. In Figure 6F, a bright spot appears at the release location, indicating reflections from the ethanol as it migrates downward through the vadose zone. Similar to profile 9, we also see strong reflections in the first half of the tank between 15 and 17 ns. By the end of the experiment, reflections for the first 13 ns return to prerelease conditions, but the later times show signal dampening and a phase shift relative to baseline.

Figure 7 shows the amplitude contours and individual traces at the release for saturated soil, below the water table. The most significant events occur after 15 ns, and there is evidence of refraction at the adjacent walls. Evidence of the ethanol release start to show around two hours, with events arriving slightly faster with the ethanol than without. This is due to the lower dielectric of the ethanol compared to water, allowing a faster travel time. A bright spot also appears at the two hour mark. By the end of the experiment, the timing of events have returned to baseline conditions. However, the strength of those events appear to have higher amplitudes.

The nature of this response can be explained one of three ways: first the ethanol may impact the water table, then through a LNAPL like buoyancy, rebound to the water table surface and spread laterally through the capillary fringe; second the ethanol may mix readily with the water and separate from the brilliant blue dye, leaving only the dye in the capillary zone; or finally, some of the ethanol may be retained in the porespace below the water table while the majority returned to the capillary fringe and continued to spread laterally. The photographic evidence shows only that a blue layer is established in the capillary fringe which then spreads laterally. A complementary laboratory ethanol tank study, completed at the same time as this work looks at a side by side comparison of electrical resistance tomography (ERT) imaging with time-lapse photographic imaging. The initial results from that effort show the electrical signature of ethanol present below the water table even after the photographic evidence indicates otherwise. Preliminary results are available in Glaser (2011).

To investigate the dispersive nature of the ethanol, the frequency content of the GPR traces were examined through the power spectrum. The power spectrum is simply the square of the absolute value of the Fourier transform, and was conducted on each trace after removing the mean value (DC component). Figure 8 shows the results of the log-transformed, contoured power spectra for all three profiles at two times: before ethanol release and after the cessation of the release. Figure 8A shows that for the vadose zone in dry conditions, the main signal component of the radar pulse is in the range of 400 to 1600 MHz, or one-half to double the center frequency. By the end of the experiment (Figure 8B), the power at 400 MHz has increased by about an order of magnitude and the higher frequencies have lost significant power.

To summarize and compare power spectra across time, the total power was computed through integration of each power trace. Figure 8C shows the total power across the tank, comparing

four snapshots during the release to the baseline, beginning at two hours. The total power at two hours shows a marked decrease centered at the release point, with a width of about 0.30 cm. Since the pore space is filling with a dispersive dielectric fluid, the power reduction is expected. As the release continues, we observed the spread outward to about 45 cm. Curiously, the beginning portion of the tank also sees a decrease in power, likely from the effects of reflections off the plume. By the end of the experiment at 16 hours, there is a slight recovery beneath the release but a large loss on the left side.

The power spectra of profile 21 (Figure 8D) shows much of the power in the frequency range of 600 MHz to 800 MHz, and the power is higher towards the left side of the tank. After the release (Figure 8E), the power in the left side is significantly lower than the region below the release on the other side of the tank. Based on the time-lapse photography, we interpret this as the vertical expansion of the capillary zone and mounding of the water table due to the addition of ethanol. Since this is a closed system, and the ethanol entered the system asymmetrically, there was a "loading" effect observed where the ethanol displaced the water towards the other side of the tank. Given that ethanol is a lower dielectric than water, the loading allowed a higher signal strength to penetrate the contaminated region. The total power of Figure 8F shows the history of the release, with a plume spread of about 30 cm after four hours into the release compared to a similar spread at two hours for profile 9. Relative to baseline, the ethanol plume shows a higher total power and the addition of water to the left side of the tank shows a lower total power. By 8 hours, the left half of the tank represents water and the right half represents ethanol. At 16 hours, it looks as though mixing may have occurred and there is no longer a sharp contrast at the fluid boundary.

The power spectra of profile 33 shows little change in pre and post release conditions. Both times have much lower values than those above. Figure 8I shows that the most significant change in the total power occurs beneath the release at 16 hours, after mixing of water and ethanol has decreased the dielectric.

These results indicate detection of an ethanol release in an idyllic laboratory setting is achievable through reflectivity, velocity, and power analyses, at three different levels of saturation. While we acknowledge the limitations associated with varying subsurface geologic conditions at an actual release site, we postulate that some of the negative effects associated with these limitations could be offset due to the enhanced response from biogenic gases generated through the microbial activity associated with natural attenuation of the released ethanol. For example, Comas et al., (2005), have field demonstrated the sensitivity of GPR measurements to changes in porespace gas content due to the degrading organic matter and subsequent generation of carbon dioxide in large northern peat basins. While, At hydrocarbon spill sites, McGlashan et al. (2012) show measureable changes in velocity associated with biogenic gas formation at an E10 release. Lopes de Castro and Branco (2003), also discuss the low reflectivity zones associated with vapor phase hydrocarbons and enhanced reflections associated with free and residual products directly above the water table. McNaughton (2011) observed a shallow high reflectivity associated with an E10 release at the Borden site, and a gradual decrease in reflectivity at the periphery of the plume with time. Mosquera (2012) observed similar results with E95 at the Borden site, noting a velocity pull-up with time at 450MHz. Reduction of reflection amplitude and increasing travel-time were observed with the duration of the experiment both cases. Each example bolsters the claim of practical field deployment and successful usage of GPR to image an ethanol-specific release.

5.0 Conclusions

An ethanol target was detected using GPR within three water-saturated conditions: in the unsaturated zone, at the capillary fringe, and in the saturated zone. The GPR results indicate an ability to detect variations in reflection amplitude, two-way travel time, and power spectra when compared to a baseline dataset. The GPR reflection results suggest ethanol within the vadose zone is the most suitable target for high frequency ground penetrating radar assuming a predominantly sand matrix. The experiment also tends to confirm previous work, which suggests ethanol will reside in the capillary fringe rather than to mix readily into the groundwater, but can be retained in the effected pore space below the potentiometric surface. Overall, these results indicate that the detection of ethanol in a sand matrix at various levels of saturation can be achieved using GPR.

6.0 Acknowledgements

This work was partially funded by the U.S. EPA Office of Research and Development under student services contract EP08D00724. Although this work was reviewed by EPA and approved for presentation, it may not necessarily reflect official agency policy. Mention of trade names or commercial products does not constitute endorsement or recommendation by the EPA for use. Additional funding and equipment was provided by Idaho National Laboratory. The authors would like to thank Robert Kinoshita of Idaho National Laboratory, and Dr. Tim Johnson of Pacific Northwest National Laboratory for their assistance in the laboratory.

7.0 References

Ajo-Franklin, J.B., Geller, J.T., Harris, J.M., 2004, The dielectric properties of granular media saturated with DNAPL/water mixtures, Geophysical Research Letters, vol. 31, L17501, doi: 10.1029/2004GL020672.

Annan, A.P., 2001. Ground Penetrating Radar Workshop Notes. Ontario: Sensors and Software Inc.

Bano, M., 2006. Effects of the transition zone above a water table on the reflection of GPR waves. Geophysical Research Letters, 33, L13309, doi:10.1029/2006GL026158.

Bano, M., Loeffler, O., and Girard, J., 2009. Ground penetrating radar imaging and time-domain modeling of the infiltration of diesel fuel in a sandbox experiment. C.R. Geoscience, 341:846-858.

Benedetto, 2010. Water content evaluation in unsaturated soil using GPR signal analysis in the frequency domain. Journal of Appl. Geophy. 71, 26-35

Birken, R. and R. Versteeg (2000). Use of four dimensional ground penetrating radar and advanced visualization methods to determine sub surface fluid migration, Journal of Applied Geophysics 43: 215-226.

Borrow, D., Petroff, T., Tandon, R., and Sayer, M., 1997. Characterisation of thick lead zirconate titanate films fabricated using a new sol-gel based process. Journal of Applied Physics, 81(2):876-881.

Carcione, J.M., 1996. Ground-penetrating radar: wave theory and numerical simulation in lossy anisotropic media, Geophysics, 61(6):1664-1677.

Chen, Y., and Or, D., 2006. Geometrical factors and interfacial processes affecting complex dielectric permittivity of partially saturated porous media. Water Resour. Res., 42, WD6423, doi:10.1029/2005WR004744.

Comas, X., Slater, L., and Reeve, A., 2005. Spatial variability in biogenic gas accumulations in peat soils is revealed by ground penetrating radar (GPR). Geophysical Research Letters, 32(8), L08401, doi: 10.1029/22004GL022297.

Conyers, L.B., and Goodman, D., 1997. Ground Penetrating Radar: An Introduction for Archaeologists. AltaMira Press, Walnut Creek London and New Delhi.

Corseuil, H.X., Hunt, C.S., Dos Santos, R.C., and Alvarez, P.J.J., 1998. The influence of the gasoline oxygenate ethanol on aerobic and anaerobic BTX biodegradation. Wat. Res., 32(7):2065-2072.

Cosenza, P., Camerlynck, P., and Tabbagh, A., 2003. Differential effective medium schemes for investigating the relationship between HF relative dielectric permittivity and water content of soils. Water Resour. Res., 39, 1230, doi:10.1029/2002WR001774.

Davis, J.L., and Annan, A.P., 1989. Ground-penetrating radar for high resolution mapping of soil and rock stratigraphy, Geophysical Prospecting, 37:531-551.

Da Silva, M. L. B., and P. J. J. Alvarez, 2002. Effects of ethanol versus MTBE on BTEX migration and natural attenuation in aquifer columns, J. Environ. Eng., 128(9), 862 – 867.

Doolittle, J.A., and Collins, M.E., 1995. Use of soil information to determine application of ground-penetrating radar. Journal of Applied Geophysics, 33:101-108.

Endres, A.L., and Bertrand, E.A., 2006. A pore-size scale model for the dielectric properties of water-saturated clean rocks and soils. Geophysics, 71(6): F185-F193.

Endres, A., and R. Knight (1992), A theoretical treatment of the effect of microscopic fluid distribution on the dielectric properties of partially saturated rocks, Geophys. Prospect., 40, 307–324.

Farmani, M., H. Keers, et al., 2008. Time-Lapse GPR Tomography of Unsaturated Water Flow in an Ice-Contact Delta, Vadose Zone Journal 7(1): 272-283.

Flury, M. and Flühler, H., 1995. Tracer Characteristics of Brilliant Blue FCF. Soil Science Society of America Journal 59(1): 22-27.

Friedman, S.P., 1998. A saturation degree-dependent composite spheres model for describing the effective dielectric constant of unsaturated porous media. Water Resour. Res., 34: 2949-2961.

Frietas, J.G., 2009. Impacts of Ethanol in Gasoline on Subsurface Contamination. PhD Dissertation, University of Waterloo, Waterloo, Ontario, Canada.

Frietas, J.G., and Barker, J.F., 2009. The role of the capillary fringe and unsaturated zone on the fate of organic compounds following an oxygenated gasoline spill. American Geophysical Union, Spring Meeting 2009. Abstract #H23C-02.

Frietas, J. G., Fletcher, B., Aravena, R., and Barker, J. F., 2010a. Methane production and isotopic finger-printing in ethanol fuel contaminated sites, Ground Water, 48(6):844-857.

Frietas, J.G., Mocanu, M. T., Zoby, J.L.G., Molson, J.W., and Barker, J.F., 2010b. Migration and fate of ethanol-enhanced gasoline in groundwater: A modeling analysis of a field experiment, J. Cont. Hydrol., 119 (2011): 25-43.

Glaser, D. R., Henderson, R., Versteeg, R. J., Werkema, D. D., Kinoshita, R., and Mattson, E., 2010. Automated Time-lapse GPR Imaging of an Ethanol Release. Abstract #H23C-1197 presented at 2010 Fall Meeting, AGU, San Francisco, Calif., 13-17 Dec.

Glaser, D.R., Werkema, D.D., Henderson, R.D., Johnson, T., Versteeg, R.J., and Lane, J.W., 2011. Four Dimensional Geophysical Measurements of a Controlled Ethanol Release in Ottawa Sand. U.S.EPA Internal Report APM 253.

Greaves, R.J., Lesmes, D.P., Lee, J.M., and Toksoz, M.N., 1996. Velocity variations and water content estimated from multi-offset, ground-penetrating radar, Geophysics 61(3):683-695.

Gomez, D. E., and Alvarez, P. J. J., 2009. Modeling the natural attenuation of benzene in groundwater impacted by ethanol-blended fuels: Effect of ethanol content on the lifespan and maximum length of benzene plumes, Water Resour. Res., 45, W03409.

Haarder, E.B., Looms, M.C., Jensen, K.H., and Nielsen, L., 2011. Visualizing Unsaturated Flow Phenomena Using High-Resolution Reflection Ground Penetrating Radar. Vadose Zone Journal 10(1):84-97.

Hagrey, S.A. and Muller, C., 2000. GPR Study of pore water content and salinity in sand. Geophysical Prospecting. 48:63-85.

Henderson, R., Glaser, D. R., Johnson, T, Werkema, D.D., Versteeg, R.J., and Lane, J.W., 2010. Time-lapse Geolectrical Imaging of a Controlled Ethanol Release in Ottawa Sand. Abstract #H13G-07 presented at 2010 Fall Meeting, AGU, San Francisco, Calif., 13-17 Dec.

Irving, J. D. and Knight, R., 2006, Numerical modeling of ground-penetrating radar in 2-D using MATLAB: Computers & Geosciences, 32, 1247-1258.

Jones, S.B., and Friedman, S.P., 2000. Particle shape effects on the effective permittivity of anisotropic or isotropic media consisting of aligned or randomly oriented ellipsoidal particles. Water Resour. Res., 36:2821-2833.

Kasteel, R., Vogel, H.-J., and Roth, K, 2002. Effect of non-linear adsorption on the transport behavior of Brilliant Blue in a field soil. European Journal of Soil Science, 53:231-240.

Kenyon, W.E., 1984. Texture effects on megahertz dielectric properties of calcite rock samples. J. Appl. Phys., 55:3153-3159.

Koestel, J., Kasteel, R., Kemna, A., Esser, O., Javaux, M., Binley, A., and Vereecken, H., 2008. Imaging Brilliant Blue Stained Soil by Means of Electrical Resistivity Tomography. Vadose Zone Journal, 8(4):963-975.

Loeffler O. and Bano, M., 2004. GPR measurements in a Controlled Vadose Zone: Influence of the Water Content. Vadose Zone Journal, Vol. 3, p. 1082-1092.

Lopes de Castro, D. and Gomes Castelo Branco, R.M., 2003. 4-D ground penetrating radar monitoring of a hydrocarbon leakage site in Fortaleza (Brazil) during its remediation process: a case history, Journal of Applied Geophysics, 54(1-2): 127-144.

Lucius, J.E., Olhoeft, G.R., Hill, P.L., and Duke, S.K., 1992, Properties and hazards of 108 selected substances—1992 edition: U.S. Geological Survey Open-File Report 92–527, 554 p.

MacKay, D.M., De Sieyes, N.R., Einarson, M.D., Feris, K.P., Pappas, A.A., Wood, I.A., Jackobson, L., Justice, L.G., Noske, M.N., Scow, K.M., and Wilson, John T., 2006. Impact of ethanol on the natural attenuation of benzene, toluene, and o-Xylene in a normally sulfate-reducing aquifer. Environ. Sci. Technol. 40(19):6123-6130.

Mazella A., and Majer E., 2006. Evaluation of geophysical methods for detection of subsurface Tetrachloroethylene in controlled spill experiments. SGE Abstract 25, 1466.

McDowell, C.J., Buscheck, T, and Powers, S.E., 2003. Behavior of gasoline pools following a denatured ethanol spill. Ground water, 41(6): 746-757.

McNaughton, C.H., Mosquera, J.D., Endres, A.L., and Freitas. J.G., 2009. Monitoring of Sequential Gasoline-Ethanol Releases using High Frequency Ground Penetrating Radar, GPR'09, Thirteenth International Conference on Ground Penetrating Radar, Lecce, Italy.

McNaughton, C.H., 2011. Monitoring a Shallow Gasoline Release using GPR at CFB Borden. Master's Thesis, University of Waterloo, Waterloo, Ontario, Canada.

McGlashan, M.A., Tsoflias, G.P., Schilling, P.C., Devlin, J.F., and Roberts, J.A., 2012. Field GPR Monitoring of Biostimulation in Saturated Porous Media. Journal of Applied Geophysics, 78:102-112.

Mosquera, J., 2012. High-Resolution Geophysical Characterization of an Ethanol Release into an Existing Gasoline-Impacted Zone. Master's Thesis, University of Waterloo, Waterloo, Ontario, Canada.

Olver, A.D., and Cuthbert, L.G., 1988. FMCW radar for hidden object detection, IEEE Proceedings, 135(F4): 354-361.

Orbey, H, and Sandler, S.I., 1998. Modeling Vapor-Liquid Equilibria: Cubic Equations of State and Their Mixing Rules. Cambridge University Press, Cambridge, MA.

Personna, Y.R., Slater, L.D., Ntarlagiannis, D., Werkema, D.D., Glaser, D.R., and Szabo, Z., 2011a. Observing Ethanol Degredation Using Geophysical Methods: Implications for MointoringFuel-Ethanol Release and Migration in the Subsurface. International Symposium on Bioremediation and Sustainable Environmental Technologies, Reno, NV, 27-30 June.

Personna, Y.R., Slater, L.D., Ntarlagiannis, D., Werkema, D.D., Glaser, D.R., and Szabo, Z., 2011b. Geophysical Monitoring of Biofuels Biodegradation in the Near Surface. Proceedings of the Symposium on the Application of Geophysics to Environmental and Engineering Problems, Charleston, SC, 10-14 April.

Powers, S.E., Rice, D., Dooher, B., and Alvarez, P.J.J., 2001. Will ethanol-blended gasoline affect groundwater quality? Environ. Sci. Technol., 35(1):23a-28a.

Reynolds, J.M., 1997. An Introduction to Applied and Environmental Geophysics. John Wiley & Sons, New York, NY.

Roth, K., R. Schulin, H. Fluhler, and W. Attinger (1990), Calibration of time domain reflectometry for water content measurement using a com- posite dielectric approach, Water Resour. Res., 26, 2267–2273.

Rucker, D.F. and Ferré, T.P.A., 2003. Near-Surface Velocity Estimation using Critically Refracted Waves with Borehole Ground Penetrating Radar. Vadose Zone J. 2(2):247-252.

Rucker, D.F., and Ferré, T.P.A., 2004. Automated Water Content Reconstruction of Zero-Offset Borehole Ground Penetrating Radar Data Using Simulated Annealing. Journal of Hydrology, 309:1-16.

Rucker, D.F., 2011. A FDTD modeling approach to investigate critical refraction from crosswell radar. Journal of Environmental and Engineering Geophysics 16(2):61-71.

Ruiz-Aguilar, G.M.L., K. O'Reilly, and Alvarez, P.J.J., 2003. A Comparison of Benzene and Toluene Plume Lengths for Sites Contaminated with Regular vs. Ethanol-Amended Gasoline Ground Water Monitoring & Remediation 23(1):48-53.

Sen, P.N., Scala, C., Cohen, M.H., 1981. Relation of certain geometrical features to the dielectric anomaly of rocks. Geophysics, 46(12):1714-1720.

Sen, P.N., Chew, W.C., and Wilkinson, D., 1984. Dielectric enhancement due to geometrical and electrochemical effects. In, Physics and Chemistry of Porous Media, Johsnon, D.L. and Sen, P.N., Eds. AIP Conf. Proc. 107.

Shen, L.C., Savre, W.C., Price, J.M. and Athavale, K., 1985. Dielectric properties of reservoir rocks at ultra-high frequencies. Geophysics, 50: 692-704.

Stallard, W.M., Herbert, B., Choi, H-C., and Corapcioglu, M.Y., 1997. Enhanced migration of gasohol fuels in clay soils and sediments. Environmental & Engineering Geoscience, 3(1):45-54.

Tyc, S., Schwartz, L.M., Sen, P.M., and Pozen, W., 1988. Geometrical models for the high-frequency dielectric properties of brines saturated satndstones. J. Appl. Phys. 64:2575-2582.

Versteeg, R. (2004). Time-lapse geophysics for mapping fluid flow in near real time: results from a controlled mesoscale experiment. Aquifer Characterization - SEPM Special Publication No.80, SEPM: 93-106.

Versteeg, R. and R. Birken (2001). An automated facility to study processes using 4D GPR. SAGEEP 2001, Denver, Colorado, Society of Environmental and Engineering Geophysics.

Werkema, D.D., Jackson, M., and Glaser, D.R., 2010. The Environmental Geophysics Web Site and Geophysical Support System (GDSS). U.S. Environmental Protection Agency, Washington, DC, EPA/600/C-10/004. www.epa.gov/esd/cmb/GeophysicsWebsite/index.html

Wightman, W. E., Jalinoos, F., Sirles, P., and Hanna, K. (2003). "Application of Geophysical Methods to Highway Related Problems." Federal Highway Administration, Central Federal Lands Highway Division, Lakewood, CO, Publication No. FHWA-IF-04-021, September 2003.

Wheals AE, Basso LC, Alves DMG, Amorim HV, 1999. Fuel ethanol after 25 years. Trends Biotechnol 17:482–487.

Yoon, D-H, Zhang, J., and Lee, B.I., 2003. Dielectric constant and mixing model of BaTiO3 composite thick films. Materials Research Bulletin, 38:765-772.

Figure Captions

Figure 1. Computed reflection coefficients and quality ratings for conditions presented Table 2.

Figure 2. a) Plan view schematic of the tank set up indicating line source injection point, materials, and antenna placement. b) Side view schematic indicating line source location and

relative profile locations. Note that the side view is from the south side of the tank, while the results presented below are from the north side of the tank, thus a mirror image should be considered when comparing these results. c) Photograph of the construction of the line source injection point. d) Photograph of the gantry acquisition system, control unit, and tank configuration.

Figure 3. Time lapse photography at times A through H. Profiles 9, 21 and 33 are indicated in green, red, and blue respectively. Note the blue dyed ethanol at times G and H outlined in yellow.

Figure 4. FDTD modeling of simulated tank with 800 MHz antennas and TX/RX separation of 0.1m. A) tank dimensions and labeling. B) contoured traces for a dielectric of 3.3 (dry sand). C) contoured traces for a dielectric of 6.5 (dry sand with 20% ethanol). D) contoured traces for a dielectric of 20.7 (wet sand with 5% ethanol).

Figure 5. Amplitude contours and individual traces for Profile 9 at times A-H (from 0 to 16 hours). The profile is located within the unsaturated zone. Individual traces were extracted at the release point, at 72 cm and compared to initial conditions.

Figure 6. Amplitude contours and individual traces for Profile 21 at times A-H (from 0 to 16 hours). The profile is located within the capillary fringe. Individual traces were extracted at the release point, at 72 cm and compared to initial conditions.

Figure 7. Amplitude contours and individual traces for Profile 33 at times A-H (from 0 to 16 hours). The profile is located below the water table. Individual traces were extracted at the release point, at 72 cm and compared to initial conditions.

Figure 8. Power spectra and total power for ethanol release experiment. A) power spectra for profile 9 before release. B) power spectra for profile 9 after release. C) Total power in profile 9 for five snapshots during the release experiment. D) power spectra for profile 21 before release. E) power spectra for profile 21 after release. F) Total power in profile 21 for five snapshots during the release experiment. G) power spectra for profile 33 before release. H) power spectra for profile 33 after release. I) Total power in profile 33 for five snapshots during the release experiment.

Table 1. Common electrical and electromagnetic properties for materials in the synthetic reflection models (Rucker and Ferré, 2003; Wightman et al., 2003; Werkema et al, 2010). Note the ethanol and ethanol with brilliant blue FCF (BB) conductivities were direct measurements as part of this study.

Material	Dielectric	Conductivity (S/m)	Velocity (mm/ns)	Attenuation Factor (dB/m)
Air	1	3.0E-15	300	5.07E-12
Ethanol	25	2.5E-04	60	8.45E-02
Ethanol /BB	25	1.5E-03	60	4.71E-01
Sand (dry, 3% moisture)	3.3	1.0E-05	165	9.30E-03
Sand (moist, 20% moisture)	10.6	7.5E-05	92	3.89E-02
Sand (wet, 40% moisture)	24.5	4.5E-04	61	1.54E-01
Water	80	5.0E-04	33	9.39E-02

Table 2. Test cases for determining target quality for reflection analysis

Case	Material	ε_r	V_m	R	T
A	air dry sand	1 3.3	300 165	0.29	0.71
B	dry sand ethanol/BB	3.3 25	165 30	0.47	0.53
C	dry sand water	3.3 80	165 34	0.66	0.34
D	wet sand air	24.5 1	61 300	0.66	0.34
E	wet sand ethanol/BB	24.5 25	61 60	0.01	0.99
F	wet sand water	24.5 80	61 34	0.29	0.71
$G_{p,c,crim}$	dry sand dry sand + 20% ethanol	3.3 7.6/6.5/7.6	165 109/118/109	0.21/0.17/.21	0.79/0.83/0.79
$H_{p,c,crim}$	moist sand dry sand + 20% ethanol	10.60 7.6/6.5/7.6	92.00 109/118/109	0.08/0.12/0.08	0.92/0.88/0.92
$I_{p,c,crim}$	wet sand moist sand + 20% ethanol	24.5 13.5/13/10.0	61 82/83/95	0.15/0.16/0.22	0.85/0.84/0.78
$J_{p,c,crim}$	wet sand wet sand + 5% ethanol	24.5 20.7/20.7/28.1	61 61/61/57	0.04/0.04/0.03	0.96/0.96/0.97

$_p$ *parallel mixing model results* $_c$ *cubic mixing model results* $_{crim}$ *CRIM mixing model results*

Figure 1

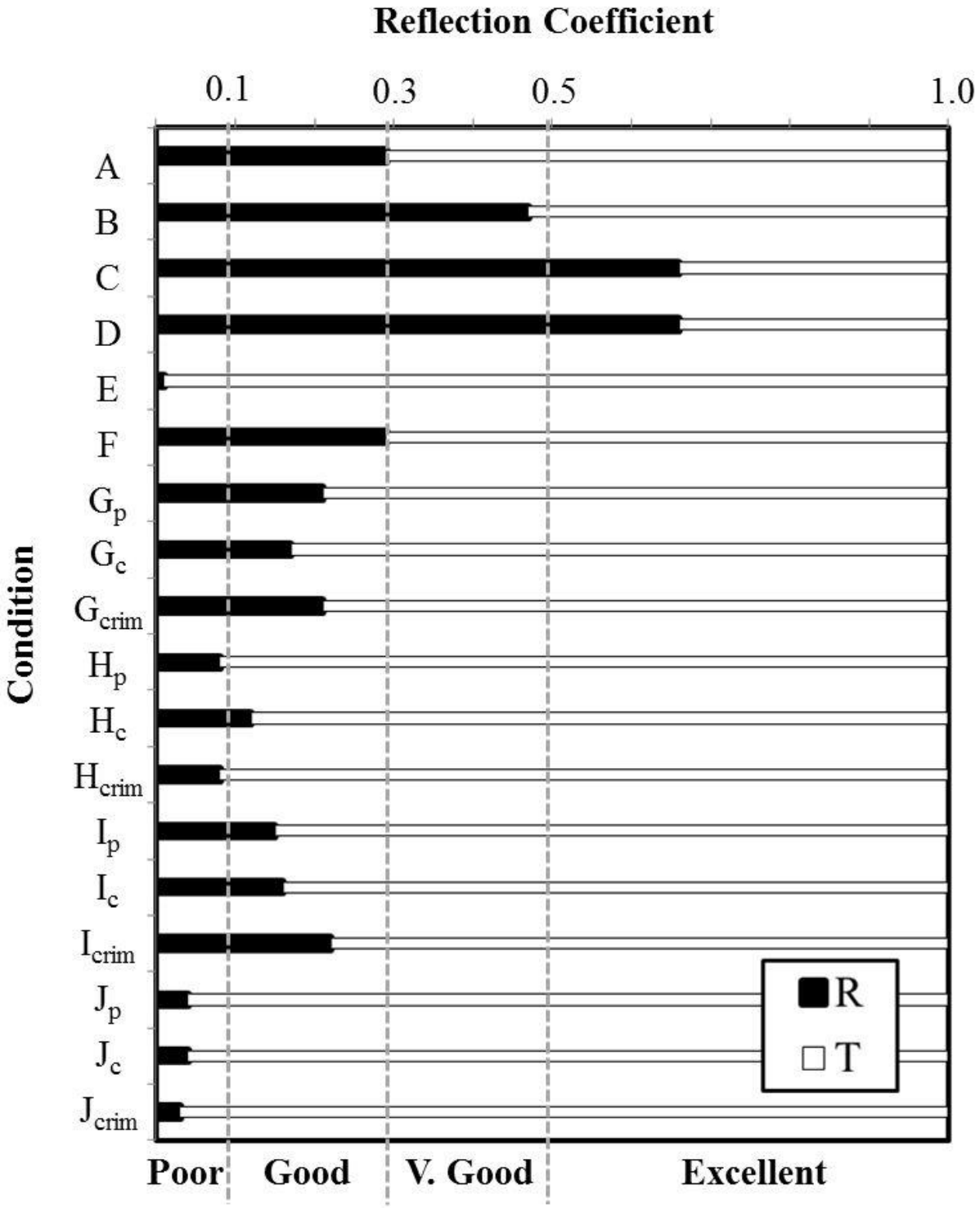
Reflection Coefficient
0.1
0.3
0.5
1.0
Condition
A
B
C
D
E
F
G_p
G_c
G_{crim}
H_p
H_c
H_{crim}
I_p
I_c
I_{crim}
J_p
J_c
J_{crim}
R
T
Poor
Good
V. Good
Excellent

Figure 2

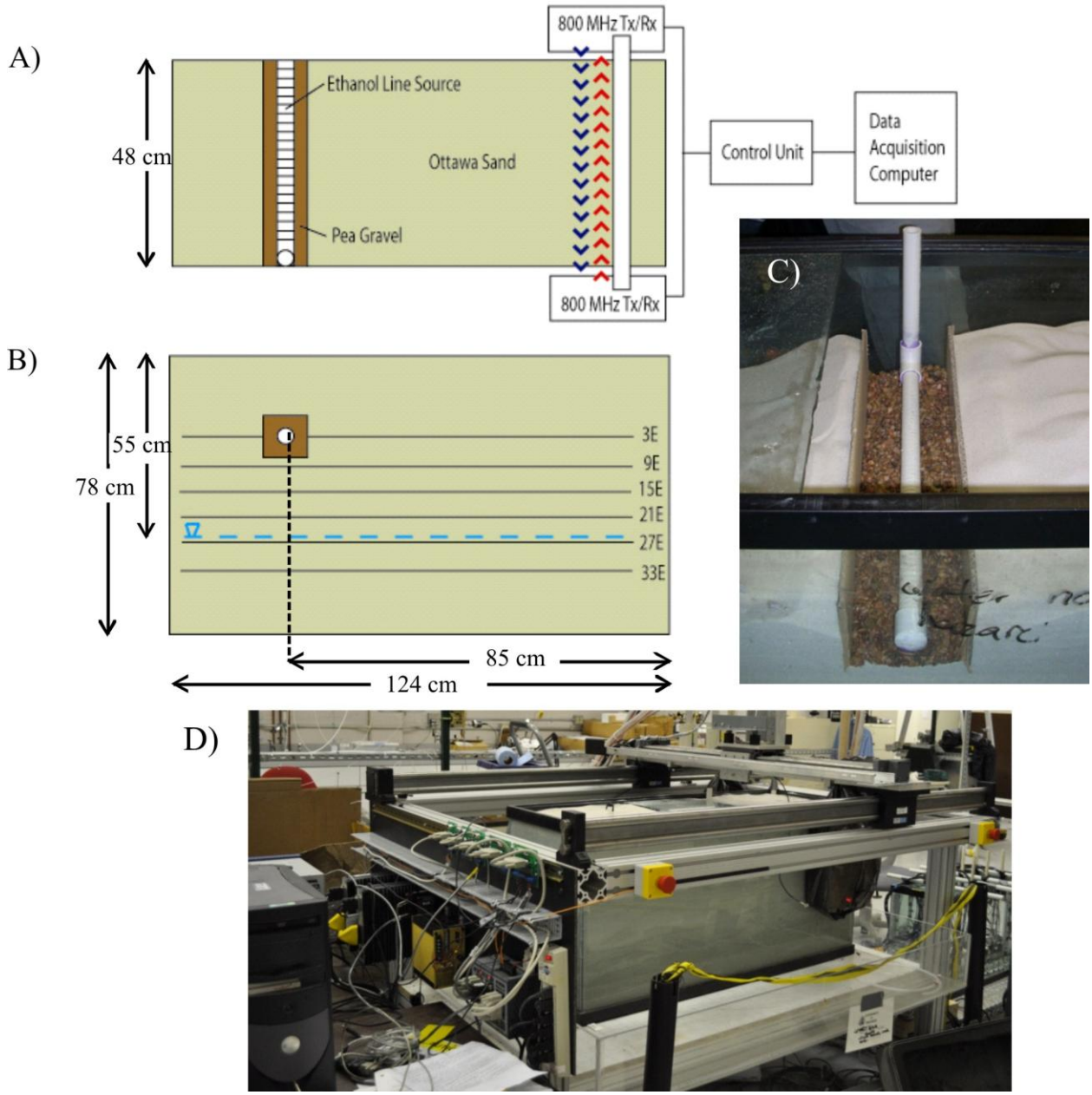
A)
800 MHz Tx/Rx
Ethanol Line Source
48 cm
Ottawa Sand
Pea Gravel
Control Unit
Data Acquisition Computer
800 MHz Tx/Rx
B)
55 cm
78 cm
3E
9E
15E
21E
27E
33E
85 cm
124 cm
C)
D)

Figure 3

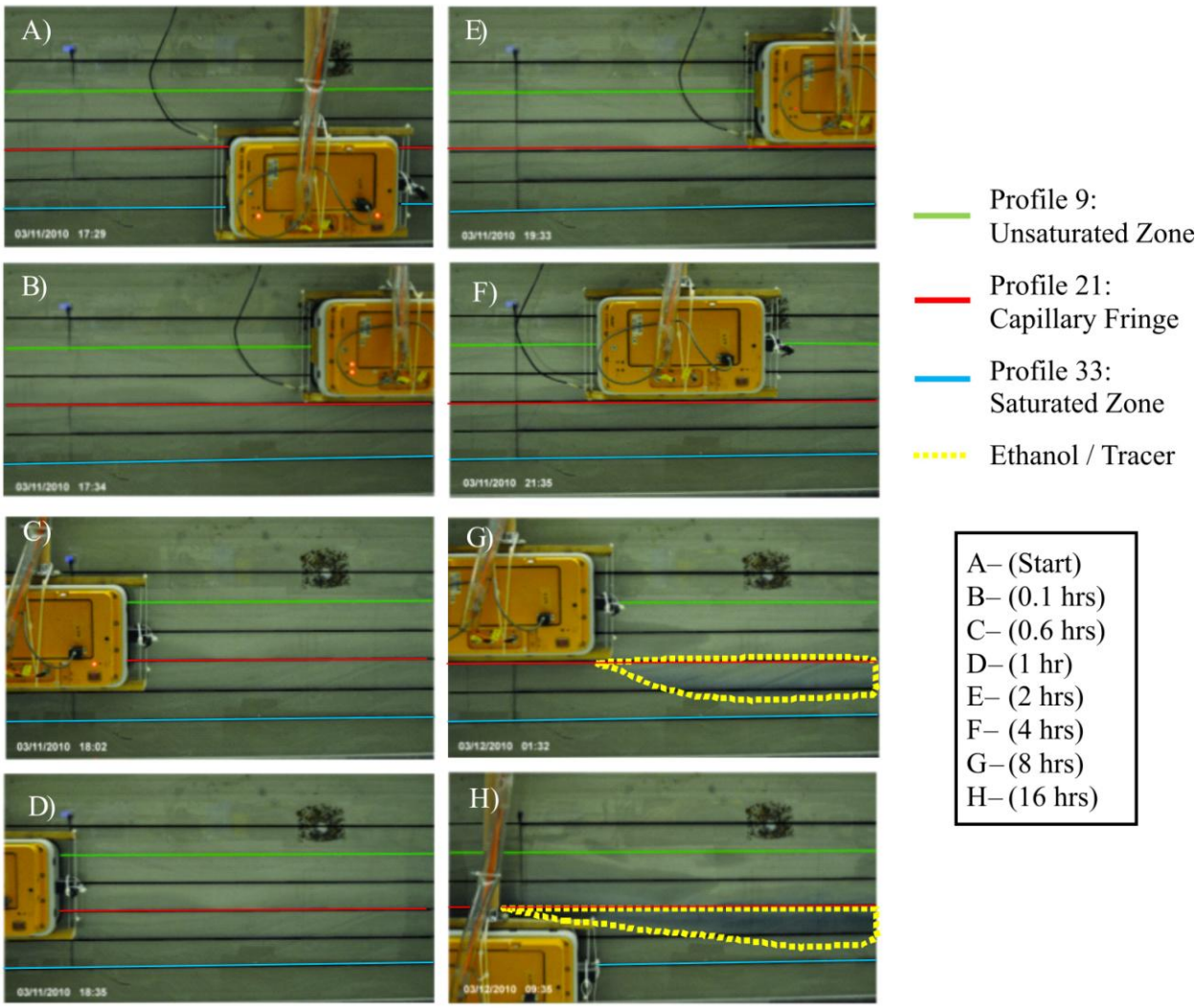
A)
03/11/2010 17:29
E)
03/11/2010 19:33
B)
03/11/2010 17:34
F)
03/11/2010 21:35
C)
03/11/2010 18:02
G)
03/12/2010 01:32
D)
03/11/2010 18:35
H)
03/12/2010 09:35
Profile 9: Unsaturated Zone
Profile 21: Capillary Fringe
Profile 33: Saturated Zone
Ethanol / Tracer
A– (Start)
B– (0.1 hrs)
C– (0.6 hrs)
D– (1 hr)
E– (2 hrs)
F– (4 hrs)
G– (8 hrs)
H– (16 hrs)

Figure 4

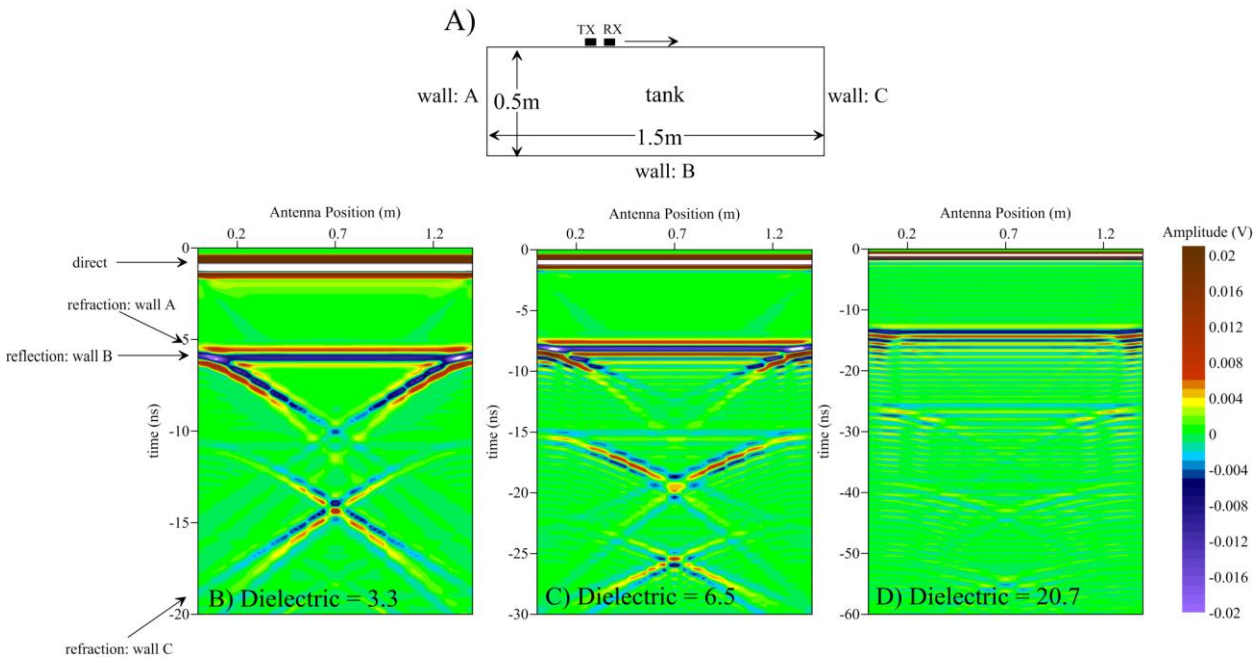
A)
TX RX
wall: A
0.5m
tank
wall: C
1.5m
wall: B
Antenna Position (m)
0.2
0.7
1.2
direct
refraction: wall A
reflection: wall B
refraction: wall C
time (ns)
B) Dielectric = 3.3
C) Dielectric = 6.5
D) Dielectric = 20.7
Amplitude (V)
0.02
0.016
0.012
0.008
0.004
0
-0.004
-0.008
-0.012
-0.016
-0.02

Figure 4

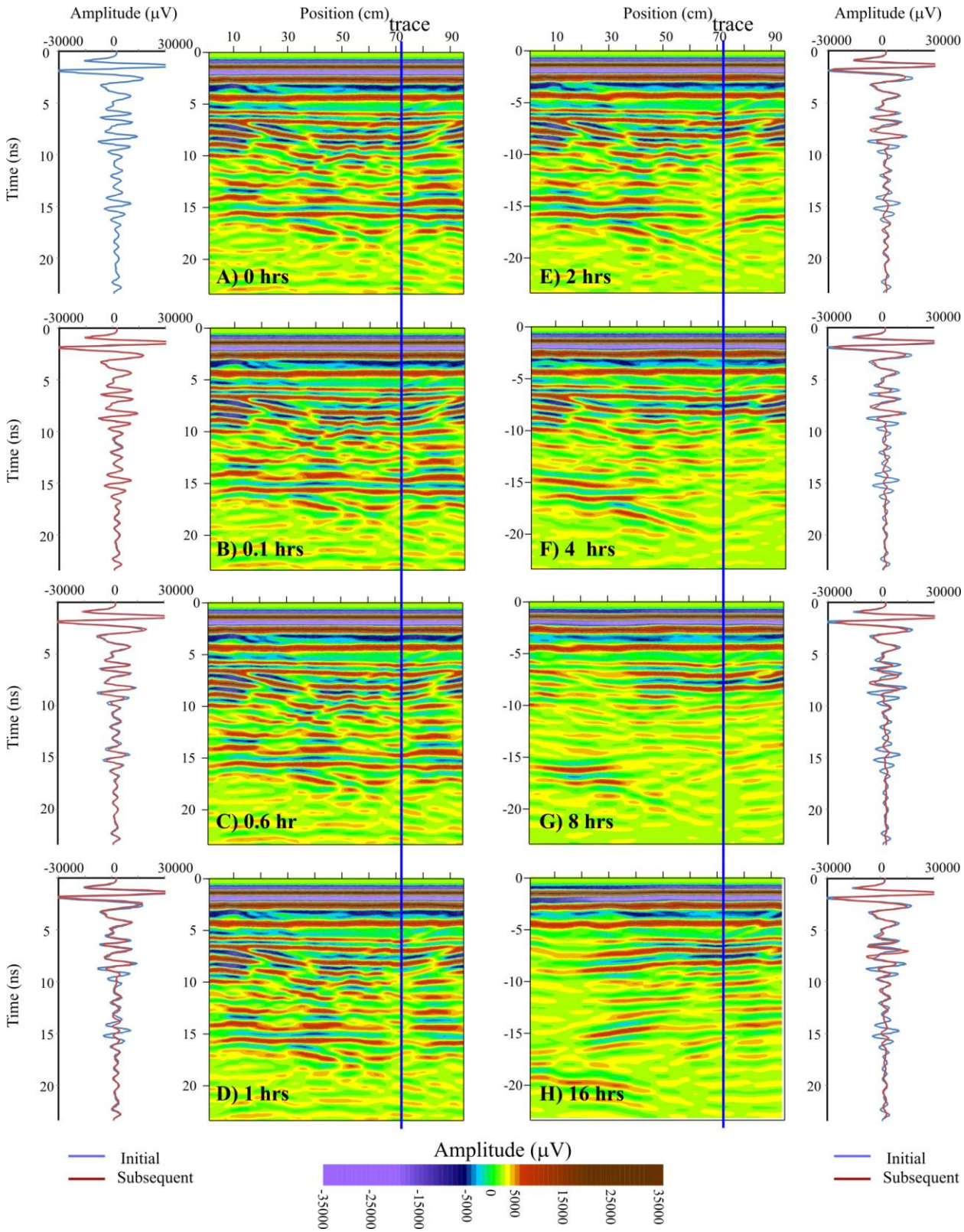
Amplitude (μV)
Position (cm)
trace
Time (ns)
A) 0 hrs
B) 0.1 hrs
C) 0.6 hr
D) 1 hrs
E) 2 hrs
F) 4 hrs
G) 8 hrs
H) 16 hrs
Initial
Subsequent
Amplitude (μV)
-35000
-25000
-15000
-5000
0
5000
15000
25000
35000

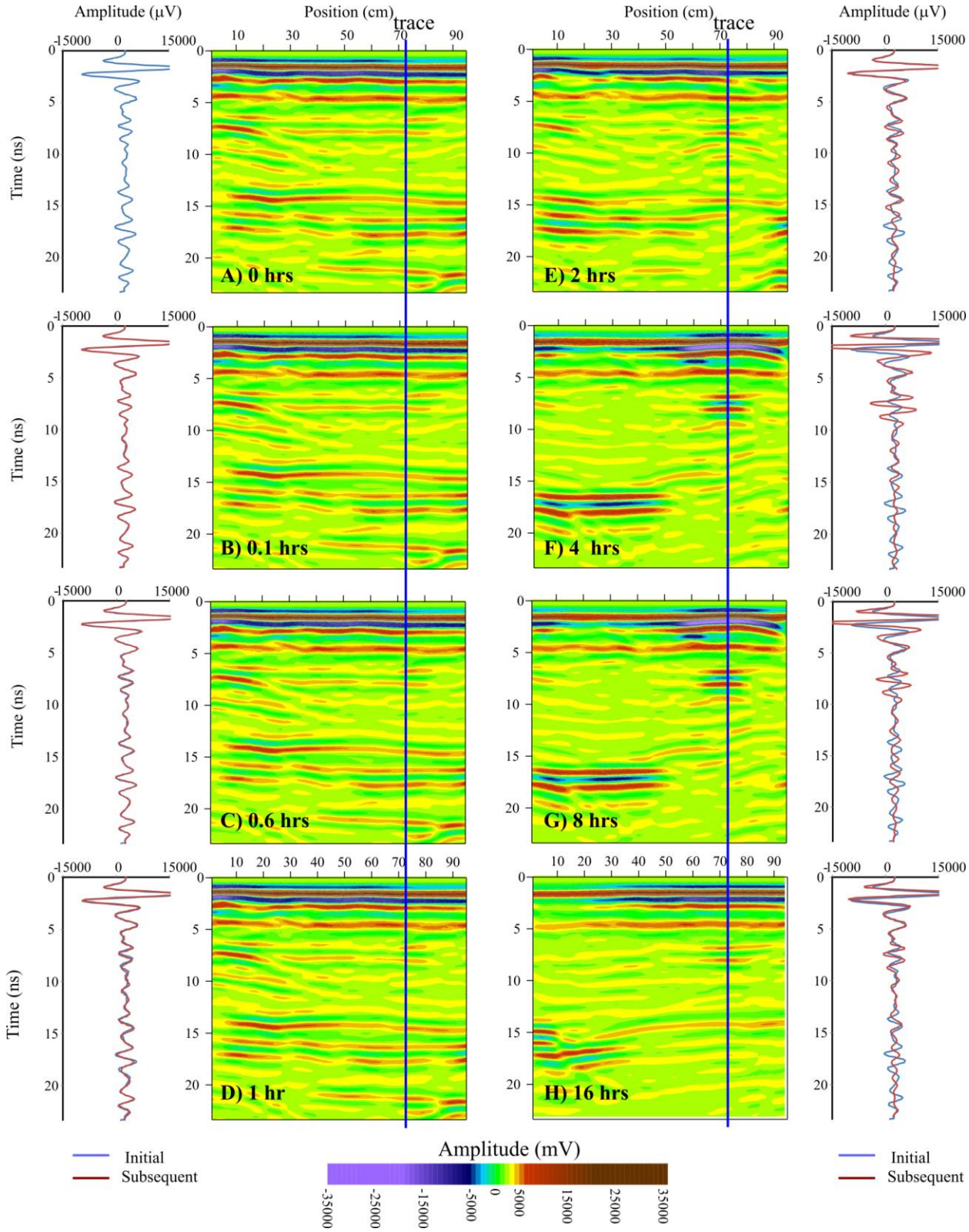
Amplitude (μV)
Position (cm)
trace
Time (ns)
A) 0 hrs
B) 0.1 hrs
C) 0.6 hrs
D) 1 hr
E) 2 hrs
F) 4 hrs
G) 8 hrs
H) 16 hrs
Initial
Subsequent
Amplitude (mV)

Figure 5

Figure 6

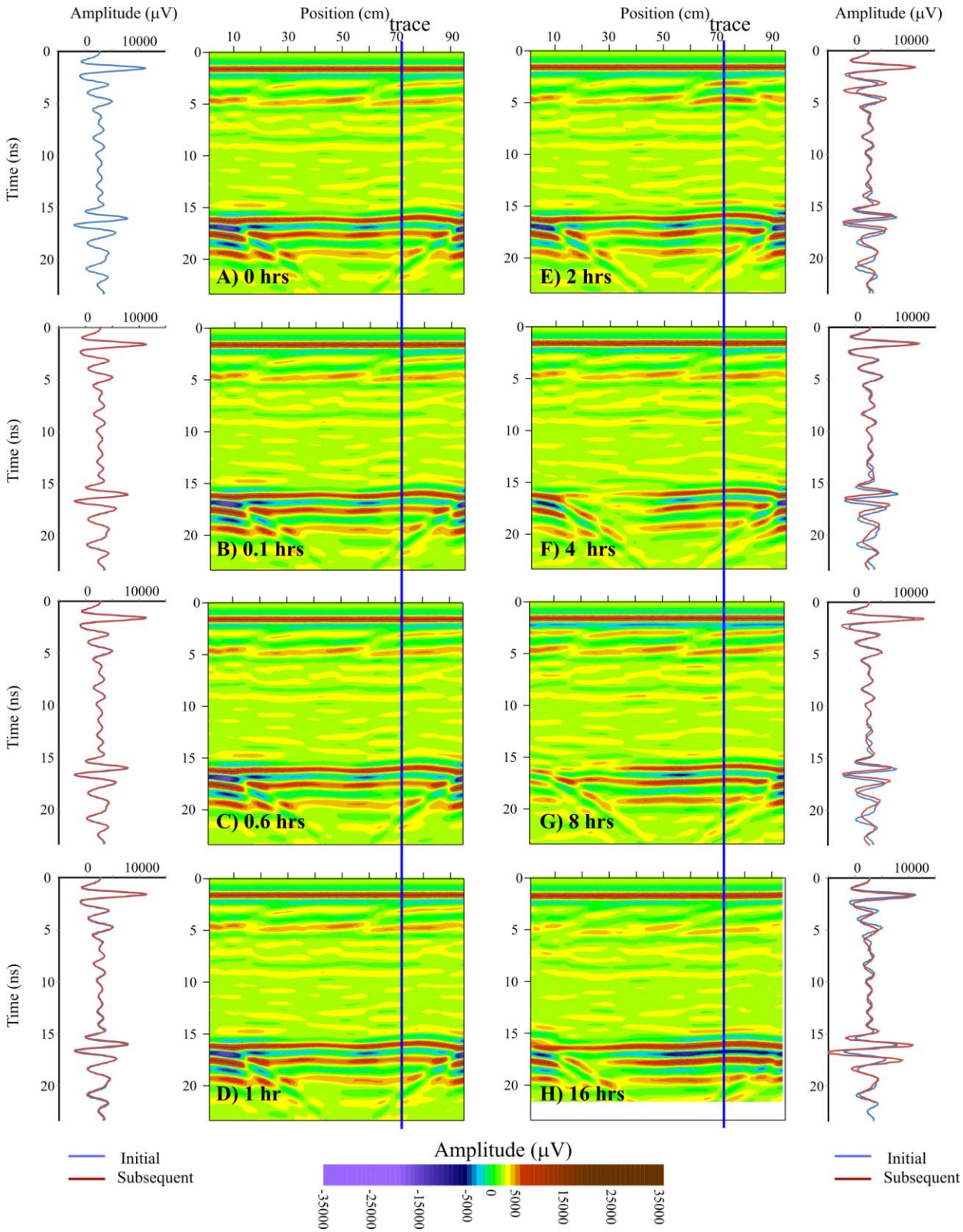
Amplitude (μV)
Position (cm)
trace
Time (ns)
A) 0 hrs
B) 0.1 hrs
C) 0.6 hrs
D) 1 hr
E) 2 hrs
F) 4 hrs
G) 8 hrs
H) 16 hrs
Initial
Subsequent
Amplitude (μV)
-35000
-25000
-15000
-5000
0
5000
15000
25000
35000

Figure 7

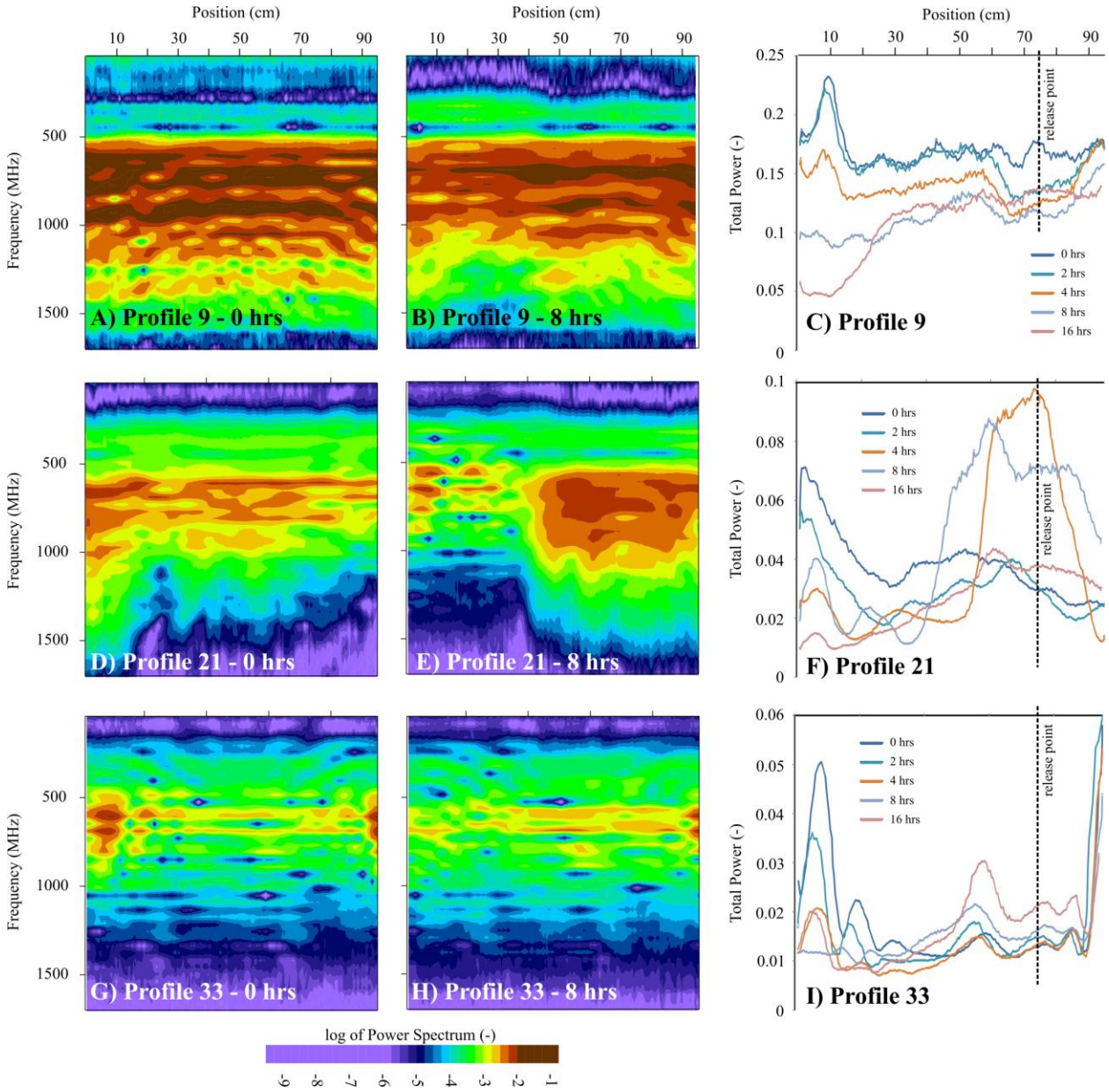
Position (cm)
Frequency (MHz)
A) Profile 9 - 0 hrs
B) Profile 9 - 8 hrs
C) Profile 9
D) Profile 21 - 0 hrs
E) Profile 21 - 8 hrs
F) Profile 21
G) Profile 33 - 0 hrs
H) Profile 33 - 8 hrs
I) Profile 33
Total Power (-)
release point
0 hrs
2 hrs
4 hrs
8 hrs
16 hrs
log of Power Spectrum (-)

Figure 8

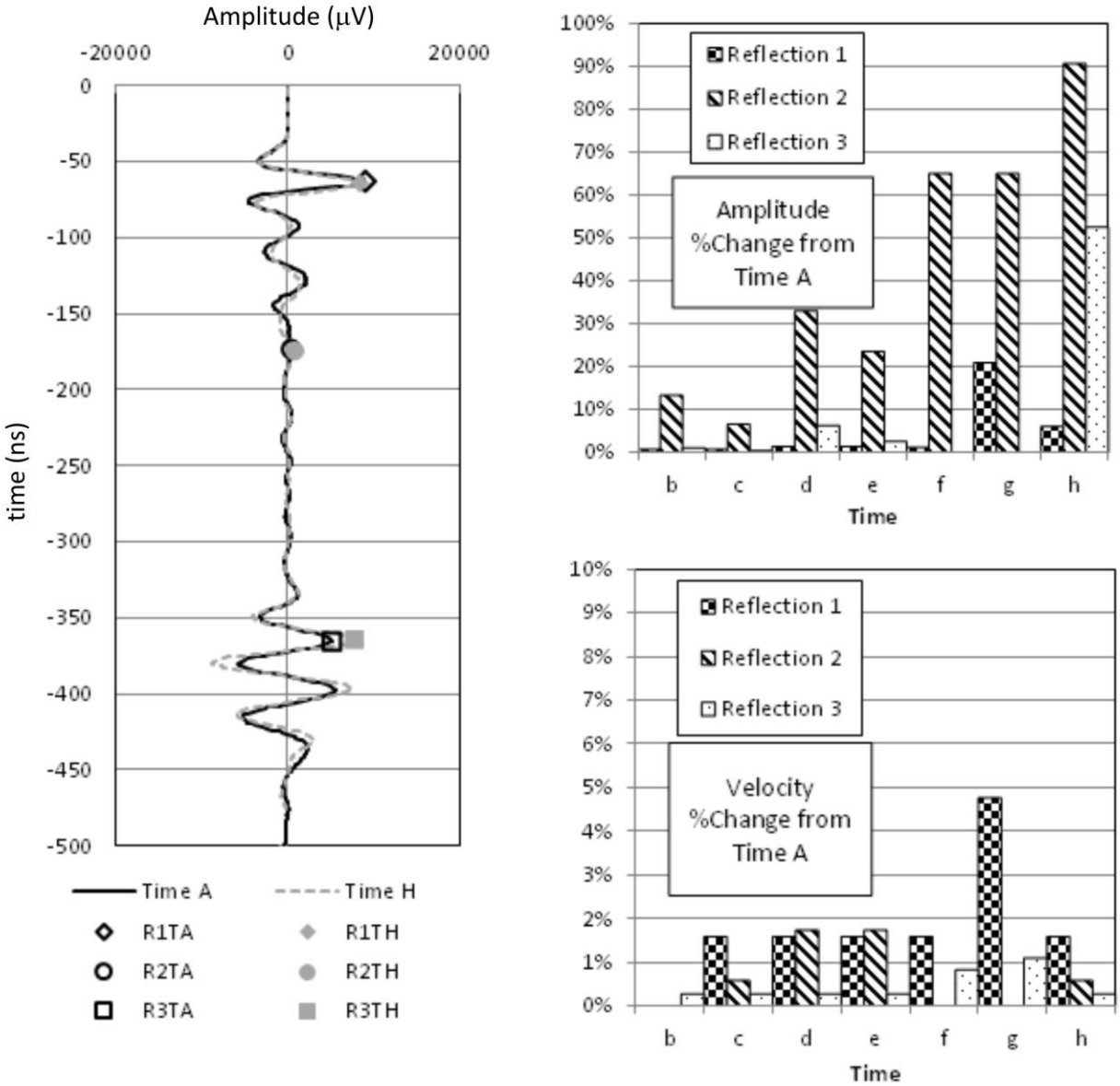
Amplitude (μV)
-20000
0
20000
time (ns)
0
-50
-100
-150
-200
-250
-300
-350
-400
-450
-500
Time A
Time H
R1TA
R1TH
R2TA
R2TH
R3TA
R3TH
100%
90%
80%
70%
60%
50%
40%
30%
20%
10%
0%
Reflection 1
Reflection 2
Reflection 3
Amplitude %Change from Time A
b
c
d
e
f
g
h
Time
10%
9%
8%
7%
6%
5%
4%
3%
2%
1%
0%
Reflection 1
Reflection 2
Reflection 3
Velocity %Change from Time A
b
c
d
e
f
g
h
Time